A Climatology of Central American Gyres

PHILIPPE P. PAPIN, LANCE F. BOSART, AND RYAN D. TORN

Department of Atmospheric and Environmental Sciences, University at Albany, State University of New York, Albany, New York

(Manuscript received 25 October 2016, in final form 11 February 2017)

ABSTRACT

Central American gyres (CAGs) are large, closed, cyclonic circulations that occur during the rainy season (May–November), which can yield exceptional rainfall leading to catastrophic flooding and large societal impacts. A reanalysis-based climatology of CAGs is developed from an algorithm that distinguishes CAG cases from other systems. This algorithm identified CAG cases based on circulation intensity, a broad radius of maximum winds, and the existence of closed, Earth-relative, cyclonic flow. Based on these criteria, 47 CAG cases were identified from 1980 to 2010, featuring a bimodal distribution of cases with maxima in May–June and September–November.

CAG cases are composited into two categories based on their upper-tropospheric PV structure: nonbaroclinic CAGs are more common ($N = 42$) and characterized by an upper-tropospheric anticyclone, while baroclinic CAGs are less common ($N = 5$) and characterized by an upper-tropospheric trough. Whereas a nonbaroclinic CAG has anomalous moisture and precipitation surrounding the center, a baroclinic CAG has anomalous moisture and precipitation concentrated east of the center, with these structural differences attributed to their upper-tropospheric PV structure. Both nonbaroclinic and baroclinic CAGs are preceded by anomalous westerly lower-tropospheric flow in the eastern Pacific before their development, which is linked to a climatological reduction in easterly trade winds and is coincident with MJO phases 1, 2, and 8. Extreme precipitation is observed over multiple days in all available CAG cases, most commonly along the Central American coastline and on average over a large fractional area (25%) within 10° of their center.

1. Introduction

Central American gyres (CAGs) are broad lower-tropospheric cyclonic circulations occurring near Central America, and are similar to broad monsoonal low pressure systems (MLs) in other oceanic basins (e.g., Boos et al. 2015; Hurley and Boos 2015). While MLs have been studied the most extensively in the north Indian Ocean basin (e.g., Piddington 1876; Eliot 1900; Krishnamurti et al. 1975; Godbole 1977; Sanders 1984; Douglas 1992; Boos et al. 2015), similar cyclonic circulations have been identified in the southern Indian Ocean basin (e.g., Davidson and Holland 1987; Baray et al. 2010), and western Pacific basin (e.g., Lander 1994; Harr et al. 1996; Aldinger and Stapler 1998; Molinari and Vollaro 2012; Beattie and Elsberry 2013; Crandall et al. 2014). The purpose of this research is to document the climatological structure and frequency of CAGs (i.e., MLs near Central America), which has mostly been documented through case studies (e.g., Lawrence 1998; Pasch and Roberts 2006; Aiyyer and Molinari 2008; Brennan 2010; Blake 2011; Montgomery et al. 2012).

MLs are often placed in one of two categories: monsoon depressions (MDs) and monsoon gyres (MGs). The American Meteorological Society's *Glossary of Meteorology* notes that MDs and MGs possess loosely organized deep convection while maintaining a circular, closed, vortex characterized by a broad low-level radius of maximum winds (RMW) (Aldinger and Stapler 1998; American Meteorological Society 2016a,b). These ML categories are distinct from tropical cyclones (TCs), which are characterized by smaller RMWs (Kimball and Mulekar 2004), and from monsoon troughs (MTs), which have cyclonic winds, but do not have a closed vortex (Lander 1994). In addition to their broad lower-tropospheric cyclonic circulation, MDs also possess a similar-scale upper-tropospheric anticyclonic circulation (i.e., low PV) (Boos et al. 2015; Hurley and Boos 2015). In contrast, MGs are associated with an upper-tropospheric trough that features a positive PV anomaly to the northwest of the lower-tropospheric cyclonic

Corresponding author e-mail: Philippe P. Papin, ppapin@albany.edu

DOI: 10.1175/MWR-D-16-0411.1

circulation (Lander 1994; Crandall 2012; Molinari and Vollaro 2012). This upper-tropospheric structure contributes to convective asymmetry, where convective activity is focused primarily south and east of the lower-tropospheric circulation center (e.g., Lander 1994; Holland 1995; Molinari and Vollaro 2012; Crandall 2012; Crandall et al. 2014). Presently, there is little insight into whether MLs over Central America (CAGs) bear greater resemblance to MDs or MGs.

Previous case studies have documented broad lower-tropospheric cyclonic circulations with CAG characteristics over Central America (e.g., Fernandez and Barrantes 1996; Lawrence 1998; Aiyyer and Molinari 2008; Blake 2011; Montgomery et al. 2012). Fernandez and Barrantes (1996) investigated the development of a broad lower-tropospheric cyclonic circulation over Central America that was associated with widespread convection and heavy rainfall in May 1982. Aiyyer and Molinari (2008) investigated the development of a broad lower-tropospheric cyclonic circulation in September 1998 that they described as a *cyclonic gyre*, which formed in response to the convectively active phase of the MJO (Madden and Julian 1971) over Central America, and later became a TC (Frances in 1998) over the Gulf of Mexico (Lawrence 1998; Pasch et al. 2001). During the 2010 Pre-Depression Investigation of Cloud-Systems in the Tropics (PREDICT; Montgomery et al. 2012) experiment, a similar broad lower-tropospheric cyclonic circulation developed over Central America and later became a TC (Nicole in 2010) at 1200 UTC 28 September (Blake 2011) over the Caribbean Sea. This system was associated with an unusually large RMW and multiple relative vorticity maxima within a broader cyclonic circulation. In addition, widespread heavy rainfall accompanied this system, with >200 mm of rain falling over a large area across Central America, Jamaica, and Cuba between 23 September and 1 October that resulted in >90 fatalities (Brennan 2010; Blake 2011). It is not known how frequently heavy rainfall occurs in association with CAGs, which can have major societal impacts (e.g., Pasch and Roberts 2006; Brennan 2010; Blake 2011).

The existing literature has contradictions on the frequency and timing of MLs over Central America during the rainy season (May–November). Hastenrath (1985, 238–240) presented a climatology of Central American *temporals*, which are loosely defined as multiday periods of continuous rainfall over portions of Central America during the rainy season. While temporals are not directly related to TCs, they are associated with systems possessing light wind cores that resemble the broad lower-tropospheric circulation of MLs (e.g., Fernandez and Barrantes 1996). Hastenrath (1985) noted that temporals develop approximately once per year, occurring most frequently in June and September–October, when the intertropical convergence zone (ITCZ) migrates northward. By contrast, the global ML climatology constructed by Hurley and Boos (2015) identified 4–10 MLs per year in a region encompassing Central America, with a seasonal peak in frequency in August.

The goals of this study are to document the climatological characteristics of CAGs, which includes the composite synoptic evolution of different CAG categories, the frequency of heavy precipitation associated with CAGs, and the intraseasonal variations associated with CAG activity. CAGs are identified using a new algorithm, which is introduced in section 2. Section 3 describes the frequency, composite structure, rainfall, and intraseasonal variability of CAGs. Section 4 summarizes and provides general conclusions.

2. Data and methodology

a. Datasets

CAGs are identified using four times daily (0000, 0600, 1200, and 1800 UTC) analyses from the National Centers for Environmental Prediction (NCEP) 0.5° Climate Forecast System Reanalysis (CFSR) dataset (Saha et al. 2010), between 1980 and 2010. The presence of convection associated with CAGs is confirmed using the National Climatic Data Center's (NCDCs) 8-km gridded geostationary satellite archive (GridSat; Knapp et al. 2011) sampled every 6 h. MJO phase is determined from the Wheeler and Hendon (2004) Real-time Multivariate MJO (RMM) index available from the Center for Australian Weather and Climate Research (http://www.bom.gov.au/climate/mjo/graphics/rmm.74toRealtime.txt). Rainfall associated with CAGs is obtained from the 0.25° Precipitation Estimation from Remotely Sensed Information using Artificial Neural Networks for Climate Data Record (PERSIANN-CDR; Ashouri et al. 2015), which provides daily rainfall information for the majority of the period (1983–2010). PERSIANN-CDR preforms well in cases of extreme precipitation (Ashouri et al. 2015), which combined with its long-term period of observations makes it a suitable dataset for this study.

b. Previous identification methods of MLs

Previous studies have used a wide variety of methods to identify MLs. Mooley and Shukla (1987) identified MLs in the north Indian Ocean using surface pressure anomalies, while Chen and Weng (1999) and Yoon and Chen (2005) employed combinations of the time-mean Earth-relative streamline and pressure tendency charts. Unfortunately, techniques that use surface pressure to identify MLs are problematic over Central America,

because sea level pressure can be ill-defined over complex topography. In addition, a ML's minimum pressure is often not collocated with the large-scale circulation center (Crandall 2012). Hurley and Boos (2015) developed a global climatology of MLs, using the Hodges (1995) TRACK algorithm that follows individual 850-hPa relative vorticity maxima. They define MLs as 850-hPa vorticity maxima that last ≥48 h, with a negative pressure perturbation and maximum 850-hPa wind speed that occur within 500 km of the vorticity maximum. Relative vorticity maxima are used to track features with rotation on the same horizontal scale as the grid spacing. At 50-km grid spacing, this horizontal scale is appropriate to track TCs that have characteristically small RMWs. By contrast, MLs possess a broad axis of rotation that is associated with a large RMW, which occasionally have smaller TC-scale vorticies embedded within (e.g., Lander 1994). As a consequence, Crandall (2012) and Crandall et al. (2014) identify a ML center via the maximum radially averaged circulation (900–1200 km; the typical size of MGs), which better represents the large-scale rotation. This method does not remove small TCs within MGs, but rather allows their vorticity to contribute to the identification of the larger-scale MG circulation. The identification algorithm described below is an extension of the Crandall (2012) and Crandall et al. (2014) technique that includes additional criteria that screen out features that do not have broad RMWs or closed Earth-relative circulations (see section 2c), and hence are not CAGs.

c. *Identification algorithm for CAGs*

This study employs an automated algorithm in order to identify CAGs that possess broad, closed Earth-relative low-level cyclonic circulations with large RMWs. CAGs are identified as maxima in 850-hPa circulation using a radial mean (100-km intervals) from 500 to 1000 km in radius. This technique is similar to Crandall (2012) and Crandall et al. (2014) which identified the center of a MG using radial mean circulation, but at larger radii (900–1200 km). Circulation is useful for identifying large-scale features because it indicates macroscopic rotation and is equivalent to area-averaged vorticity via Stokes's theorem (Holton 2004, 86–93). The radial mean (500–1000 km) of area-average vorticity (hereafter AAVORT) was chosen to be consistent with the size of MDs and MGs described in previous studies. To be characterized as a CAG, a candidate system must have a maximum AAVORT $> 1 \times 10^{-5}\,\mathrm{s}^{-1}$ for ≥48 h. The magnitude and time threshold of AAVORT is similar to the relative vorticity magnitude used in Boos et al. (2015) to identify MDs; however, these criteria emphasize systems with robust and broad cyclonic circulations.

While AAVORT identifies broad low-level cyclonic systems, it alone cannot separate CAGs from other large systems near Central America; therefore, additional criteria are needed to classify CAGs that exist for ≥48 h. Figure 1 shows three candidate systems that pass the AAVORT criteria: a subjectively identified CAG (Fig. 1, left panels; Montgomery et al. 2012), a strong TC with a broad wind field (Dean in 2007; Fig. 1, middle panels), and a broad trough (Fig. 1, right panels). All three have active convection (Figs. 1a–c), and possess an AAVORT maximum $>1 \times 10^{-5}\,\mathrm{s}^{-1}$ (Figs. 1d–f; black contours) that effectively defines the broad macroscale center of rotation, with relative vorticity maxima embedded within (Figs. 1d–f, color shading). Tangential wind (Figs. 1g–i, color shading), based on the center of each system (Fig. 1, blue circles), is used to develop additional criteria that determine if candidate systems have broad RMWs and closed Earth-relative circulations.

CAGs are separated from large TCs by evaluating the distribution of azimuthally averaged 850-hPa tangential wind (herafter $\overline{V_t}$) as a function of radius, which is defined based on a variation of the circulation theorem:

$$\overline{V_t}(r) = \frac{C(r)}{2\pi r}. \tag{1}$$

Here C is the area-averaged vorticity within the circle of radius r. A system is classified a CAG if $\overline{V_t} \geq 5\,\mathrm{m\,s}^{-1}$ and RMW ≥ 500 km. These criteria separate these systems from large TCs, which have RMWs ≪ 500 km (Kimball and Mulekar 2004). Whereas the candidate CAG has a RMW of 750 km (Fig. 1j), the RMW of TC Dean is 150 km (Fig. 1k); therefore, the latter does not qualify as a CAG. We note that this criterion does not remove all TCs, but rather large TCs whose broad circulation comprises the center point of a candidate CAG. Small TCs can be observed occasionally on the periphery of a broader CAG circulation, similar to TCs observed near MGs in prior literature (e.g., Lander 1994; Crandall et al. 2014).

One final criterion is used to separate CAGs from large-scale troughs, which do not have a closed Earth-relative circulation. The existence of a closed circulation is determined by computing average 850-hPa tangential wind in 60° arc annuli between 500 and 1000 km from the center (hereafter ArV_t). The location of the 60° arc annulus is rotated at 10° intervals for one revolution (360°) around the candidate system (36 arc annuli in total). In order for a candidate to be classified as a CAG, ArV_t must be $>1\,\mathrm{m\,s}^{-1}$ in each azimuth, which indicates a closed, cyclonic circulation exists. Of the two remaining candidate systems, the subjectively identified CAG has cyclonic flow in all azimuths (min ArV_t of $3\,\mathrm{m\,s}^{-1}$ at 240°, Fig. 1m), while the trough has

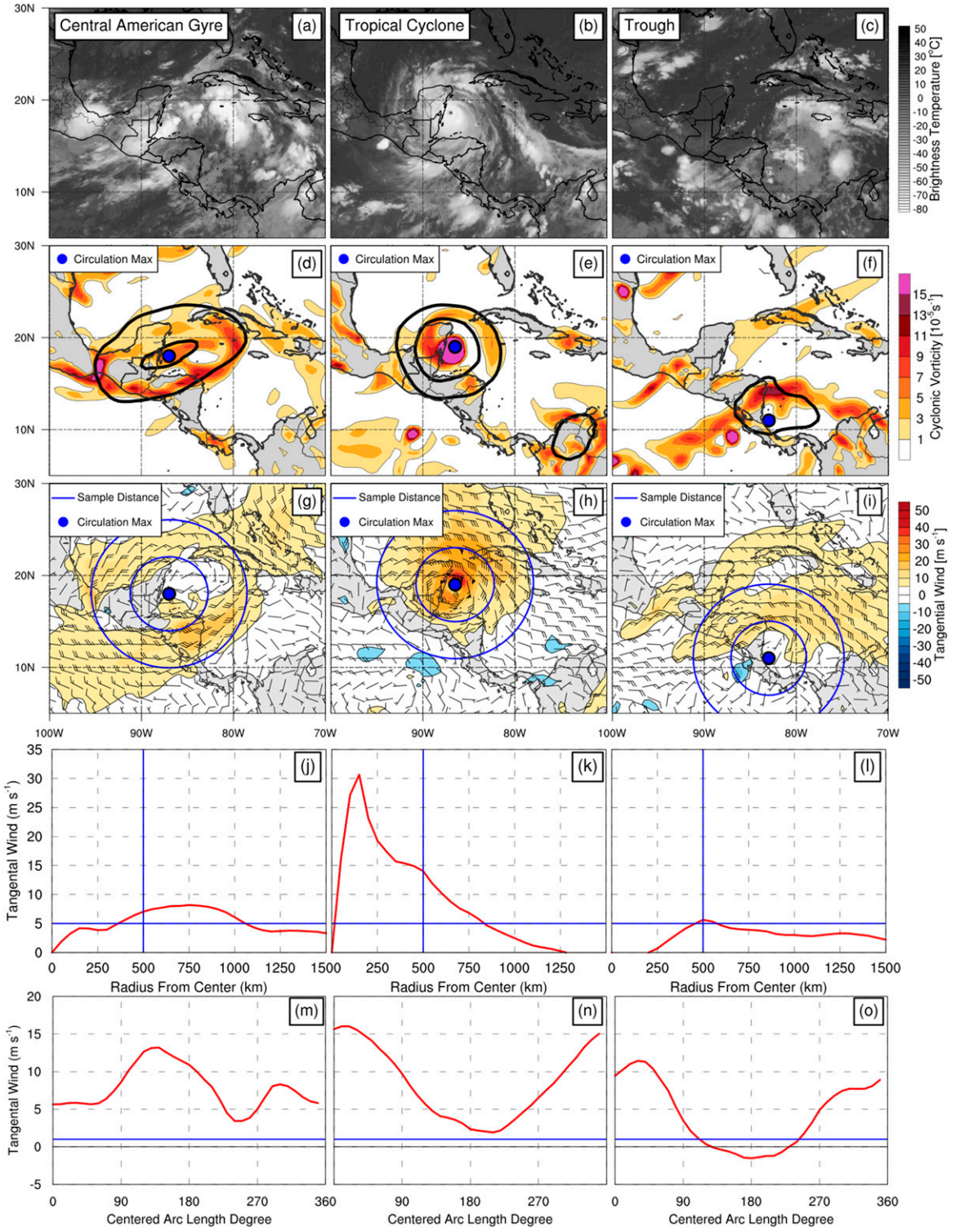

FIG. 1. CAG algorithm diagnostics for three different candidate systems: (left) 0600 UTC 28 Sep 2010, (middle) 0600 UTC 21 Aug 2007, and (right) 1200 UTC 13 Oct 2002. (a)–(c) Infrared satellite imagery depicting brightness temperature (°C, shaded). (d)–(f) 850-hPa cyclonic relative vorticity (shaded, $>1 \times 10^{-5}\,s^{-1}$) and AAVORT (black contours, $>1 \times 10^{-5}\,s^{-1}$ every $1 \times 10^{-5}\,s^{-1}$). (g)–(i) 850-hPa V_t (shaded, m s^{-1}) and total wind (barbs, kt). Blue range rings represent 500- and 1000-km distances, respectively. (j)–(l) Azimuthally averaged V_t as a function of distance from center (red line). (m)–(o) Arc averaged V_t as a function of azimuth (red line). Blue lines in (j)–(o) are threshold values used in the CAG algorithm.

TABLE 1. Sensitivity tests of CAG algorithm using variations to threshold values.

AAVORT	$\overline{V_t}$	ArV_t	Cases
0.5	5.0	1.0	51
1.0	5.0	1.0	51
1.5	5.0	1.0	40
1.0	2.5	1.0	54
1.0	7.5	1.0	25
1.0	5.0	0.5	77
1.0	5.0	1.5	33

anticyclonic flow in its southern semicircle (min ArV_t of $-2\,\mathrm{m\,s^{-1}}$ at 180°, Fig. 1o), meaning it does not have a closed cyclonic circulation, and therefore does not qualify as a CAG.

While these criteria could be applied to any geographical area, the focus of this study is on broad cyclonic circulations that occur near Central America, defined as 5°–30°N and 70°–100°W. This region covers the Gulf of Mexico, the western Caribbean Sea, and most of Central America. Moreover, only the warm season (1 May–30 November) is considered because it coincides with the Central American rainy season (Magaña et al. 1999). These criteria yield 51 CAG cases over the 31-yr period.

The number of CAG cases appear to be relatively insensitive to the threshold values employed here (Table 1). Decreasing AAVORT or $\overline{V_t}$ magnitude thresholds by 50% resulted in only minor changes to the total number of CAG identified (51 and 54 cases, respectively). By contrast, decreasing the ArV_t threshold to $0.5\,\mathrm{m\,s^{-1}}$ resulted in more potential CAGs (77 cases); however, most of the new cases resembled elongated open troughs. Increasing AAVORT, $\overline{V_t}$, and ArV_t by 50% reduces the number of CAGs identified (40, 25, and 33 cases, respectively), although at the expense of omitting previously identified CAG cases (Lawrence 1998; Pasch et al. 2001; Aiyyer and Molinari 2008).

Additional quality control measures were used to eliminate other undesired cases. Two identified cases (25 September 1980, 2 November 2001) were removed from the climatology because they represented cases where an earlier-identified CAG (20 September 1980, 28 October 2001) went below threshold criteria for a time (i.e., these cases contained two discrete ≥48-h periods). Two more identified cases (19 October 1988, 11 September 2004) are removed because they pass all criteria when a large and intense TC (Joan in 1988, Ivan in 2004) is superimposed on the outer radii of a broader cyclonic circulation that was otherwise too weak to qualify as a CAG. The added relative vorticity from the TC artificially inflates the cyclonic tangential winds at the outer radii of the weaker cyclonic circulation and produces a RMW much larger than observed in the TC. These cases are not included because the TC is the dominant feature driving the increase in the tangential wind around these systems.

The final number of CAGs identified by this algorithm (47) is much lower than the total number of MDs or stronger cases (145) identified by Hurley and Boos (2015) for the same period and geographical area; these differences are attributable to the algorithms used. For example, the AAVORT threshold ($>1\times10^{-5}\,\mathrm{s^{-1}}$) used here is stricter than the relative vorticity threshold ($>0.5\times10^{-5}\,\mathrm{s^{-1}}$) chosen in Hurley and Boos (2015) because it requires cyclonic vorticity over a relatively large area. Moreover, the Hurley and Boos (2015) algorithm may classify some TCs as MDs, because their algorithm separates candidate disturbances into various categories based on wind speed maxima in the ERA-Interim (Dee et al. 2011). This dataset can grossly under represent TC intensity, particularly in the eastern Pacific basin (Schenkel and Hart 2012), which results in some candidate systems being classified as MDs rather than *deep depressions* (Hurley and Boos 2015, see their appendix). The algorithm used here separates CAGs (large RMW) from mature TCs (small RMW) via the RMW threshold. Finally, Hurley and Boos (2015) may classify vorticity maxima associated with troughs as MDs, which do not possess closed Earth-relative circulations. The ArV_t threshold ($>1\,\mathrm{m\,s^{-1}}$) builds upon prior studies that determined closed ML circulations visually using streamlines (e.g., Chen et al. 2004; Wu et al. 2013).

d. Organization of CAG categories and composites

The CAGs identified in section 2c are further subdivided based on the distinction between MDs and MGs, which have different upper-tropospheric characteristics. Recall that MDs feature an upper-tropospheric anticyclone (i.e., low PV) (Boos et al. 2015; Hurley and Boos 2015), while MGs possess an upper-tropospheric cyclone (i.e., high PV) (Molinari and Vollaro 2012; Crandall et al. 2014). Here, CAGs are subdivided based on the nearby 350-K PV at CAG identification time. The 350-K isentropic surface is used because it is located near the tropical tropopause, and was used in western Pacific MG studies (Molinari and Vollaro 2012; Crandall 2012). Presence of a nearby trough is determined using a PV test similar to the ArV_t test, where PV is averaged in 60° arcs between 500 and 1000 km around the CAG center. Cases where PV > 2 PVU ($1\,\mathrm{PVU}=10^{-6}\,\mathrm{K\,kg^{-1}\,m^2\,s^{-1}}$) within an arc are classified as baroclinic CAGs. Based on this criteria, only 5 out of 47 (10.6%) CAGs are classified baroclinic CAGs, while the remaining 42 out of 47 (89.4%) cases

are classified as nonbaroclinic CAGs (i.e., no upper-tropospheric trough precursor).

CAG-relative composites of the nonbaroclinic and baroclinic CAG cases are employed to document the typical development and evolution of each category. Both nonbaroclinic and baroclinic CAG categories are time lagged at 48-h intervals from 2 days prior to 2 days after a system is classified. CAG-relative composites can capture the synoptic-scale features important in the evolution of each CAG category. An important caveat we stress while composing CAG-relative composites is that the baroclinic CAG composite ($N = 5$) is not as robust as the nonbaroclinic CAG composite ($N = 42$) given its much lower sample size in the CFSR climatology. Another drawback of using the CAG-relative framework is that it may smear out meteorological variables affected by moving Central American topography (geopotential height, precipitable water), though this is somewhat alleviated by employing standardized anomalies of those meteorological variables, which allow for their comparison regardless of location or period. Standardized anomalies are calculated using the formula below:

$$Z = \frac{x - \overline{x}}{\sigma}, \tag{2}$$

where x represents the mean of a variable averaged over all CAG cases at a particular location, $\overline{x}$ is the climatological mean, and σ is the climatological standard deviation of x at that location and time of year. The climatological mean and standard deviation are defined at 0000, 0600, 1200, and 1800 UTC each calendar day of the year using the first four harmonics of the CFSR 31-yr mean and standard deviation (1980–2010). Finally, statistical significance of these anomalies is diagnosed using a two-tailed Student's t test at the 95% confidence interval.

3. Climatology of Central American gyres

a. General statistics

CAGs exhibit a distinct bimodal distribution by month, with peaks in CAG occurrence in May–June (13 CAGs) and September–November (34 CAGs), while no CAGs were identified in July or August (Fig. 2a). Interestingly, the period lacking CAG activity coincides with a reduction in *temporal* frequency as discussed in Hastenrath (1985), and a relative reduction in precipitation over Central America called the *midsummer drought* (Magaña et al. 1999). By contrast, Hurley and Boos (2015) find a peak in MD activity over the same region during August. These midseason differences in ML activity between this climatology and Hurley and Boos (2015) are likely related to how MLs are identified, where the latter study is more likely to identify smaller-scale vorticity features within the ITCZ/MT in the eastern Pacific. The lack of CAGs in July–August is likely due to the evolution of the seasonal flow; this idea will be explored in section 3d.

CAG formation locations (Fig. 2b) are distributed across the east Pacific basin (12 cases), Central America (12 cases), and the Atlantic basin (23 cases), but their track density is maximized over Central America, where there is a >40% chance a CAG will occur within 500 km of 15°N, 86°W every year. The majority of baroclinic CAGs form poleward (average 19.2°N) of nonbaroclinic CAGs (average 13.2°N); this result is not surprising, because baroclinic CAGs require PV > 2 PVU on the 350-K surface, which originates at higher latitudes. General statistics of all, nonbaroclinic, and baroclinic CAGs are provided in Table 2. The average lifespan of a CAG is a little more than 3 days (74 h), with exceptional cases lasting much longer (maximum of 174 h). Moreover, the average maximum $\overline{V_t}$ is 8.6 m s^{-1} with a maximum of 15.6 m s^{-1}. The average $\overline{V_t}$ RMW for baroclinic CAGs is slightly larger than nonbaroclinic CAGs. This size difference is statistically significant at the 95% confidence interval and is consistent with the difference in size between MDs and MGs in the western Pacific (e.g., Beattie and Elsberry 2013; Wu et al. 2013). CAGs on average propagate slowly to the west-northwest (2.1 m s^{-1} at 307°). The propagation speed and direction of CAGs is similar to MDs in the Indian Ocean basin, which propagate primarily via horizontal adiabatic advection (i.e., beta drift; Boos et al. 2015). Baroclinic CAGs have a greater northward component of motion (344°) compared to nonbaroclinic CAGs (301°), which is possibly related to baroclinic CAGs interacting with upper-tropospheric troughs poleward of their center (see section 3b).

b. Composite evolution of nonbaroclinic and baroclinic CAGs

Comparing the evolution of nonbaroclinic and baroclinic CAG composites illustrates a number of critical differences in both kinematic and thermodynamic fields. Figure 3 shows the evolution of 850-hPa geopotential height and wind anomalies. Prior to and during CAG development, both composites are characterized by an area of anomalous westerly wind south of 10°N in the eastern Pacific (Figs. 3a–d). These wind anomalies are associated with a height gradient that transitions from positive height anomalies ($+0.5\sigma$) in the east and central Pacific south of 10°N to negative height anomalies (-0.5σ) northeastward toward the composite CAG center. In the nonbaroclinic CAG category, these low-level westerly anomalies gradually strengthen over time in conjunction with a westward extension of statistically significant negative height anomalies (Figs. 3a,c,e). In the baroclinic

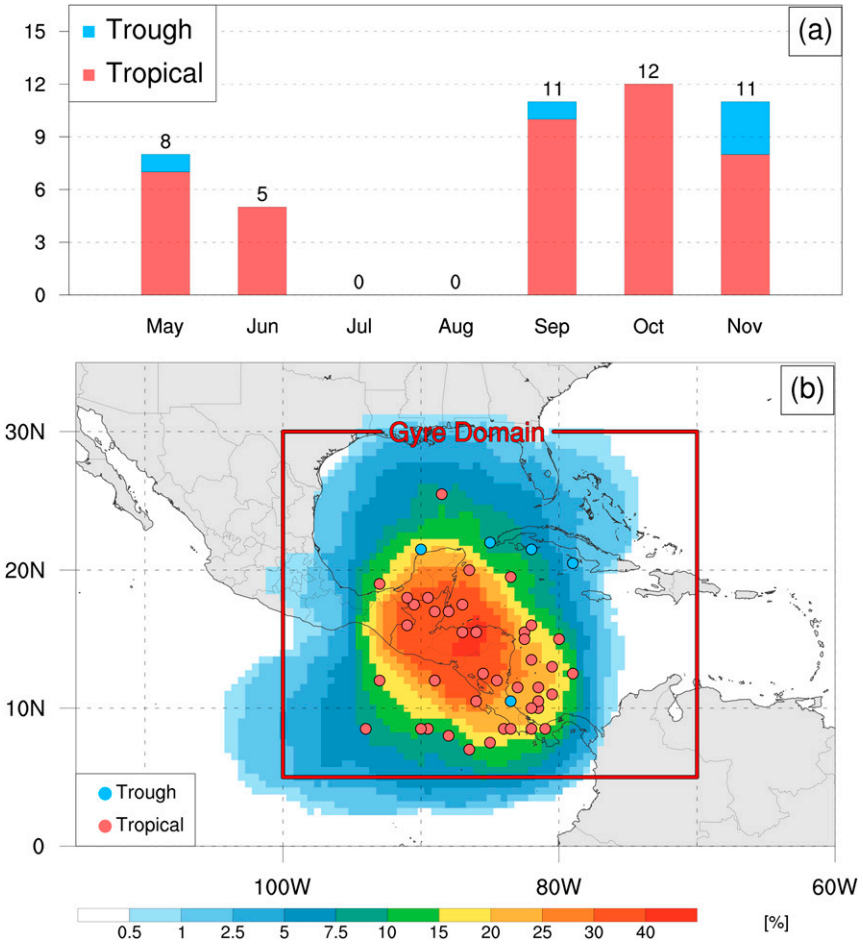

FIG. 2. (a) Monthly CAG genesis frequency (1980–2010), where red and blue colors represent the number of CAGs classified as nonbaroclinic and baroclinic events, respectively. (b) CAG locations within domain, where shading denotes probability of a CAG passing within a 500-km radius of each grid point per season (May–November). Genesis location of individual nonbaroclinic and baroclinic CAGs are shown using red and blue dots, respectively.

CAG category, easterly wind anomalies are present poleward of the Greater Antilles, in association with a height gradient between the CAG and an anomalously strong ($+0.5$–1.0σ) subtropical ridge north over the eastern United States (Figs. 3b,d,f). This enhanced subtropical ridge is not present in the nonbaroclinic CAG category. Over time, both CAG categories develop a broad circular area of statistically significant negative height anomalies ($< -1.0\sigma$) and cyclonic wind anomalies surrounding the composite CAG center; similar to the composite lower-tropospheric structure of MGs and MDs in other basins (e.g., Wu et al. 2013; Hurley and Boos 2015).

While composite nonbaroclinic and baroclinic CAGs have similar low-level mass and kinematic structures

TABLE 2. Mean CAG statistics over each set of cases. The range of values is given in parentheses.

Variable	All CAGs	Nonbaroclinic CAGs	Baroclinic CAGs
Lat at genesis (°N)	13.8 (7.0–25.5)	13.2 (7.0–25.5)	19.2 (10.5–22.0)
Lon at genesis (°W)	85.5 (79.0–94.0)	85.7 (79.0–94.0)	83.9 (79.0–90.0)
Lifespan (h)	74 (48–174)	75 (48–174)	61 (54–78)
Max azimuthally averaged wind ($m\,s^{-1}$)	8.6 (5.1–15.6)	8.6 (5.1–15.6)	8.7 (6.0–13.6)
Radius of max azimuthally averaged wind (km)	587 (500–1050)	586 (500–1050)	598 (500–775)
Propagation speed ($m\,s^{-1}$) and heading	2.1 at 307°	2.1 at 301°	2.9 at 344°

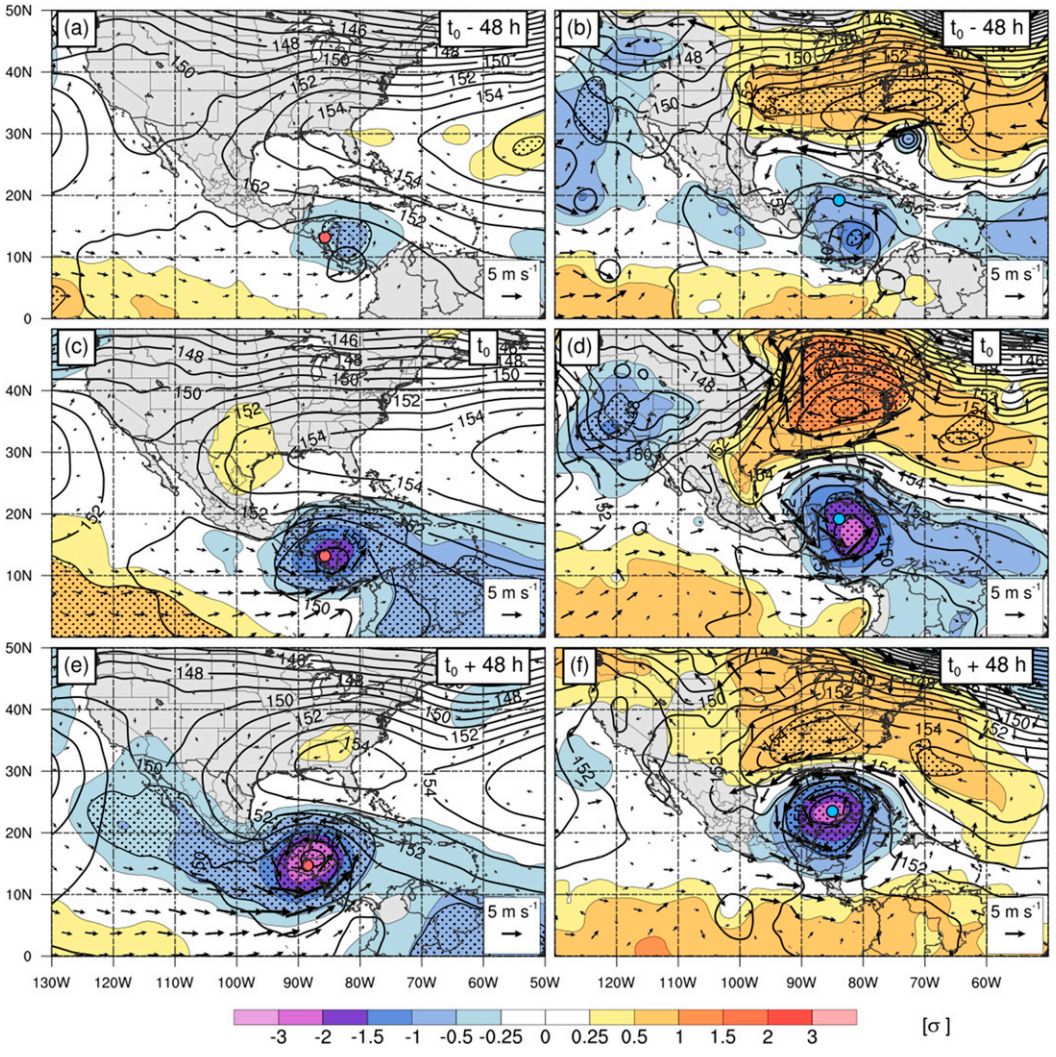

FIG. 3. CAG composite 850-hPa geopotential height (black contours, dam), standardized geopotential height anomaly (shaded, σ), and anomalous winds (vectors, m s^{-1}). The nonbaroclinic CAG composite at (a) $t_0 - 48$ h, (c) t_0, and (e) $t_0 + 48$ h. The baroclinic CAG composite at (b) $t_0 - 48$ h, (d) t_0, and (f) $t_0 + 48$ h. Red and blue circles denote the genesis points of nonbaroclinic and baroclinic CAGs, respectively, in (a)–(d), and follow the composite center CAG at $t_0 + 48$ h in (e),(f). Stippled regions denote where the 850-hPa height anomalies are statistically significant.

near the center, they exhibit vastly different moisture anomalies (Fig. 4). Prior to CAG development (Figs. 4a,b), statistically significant positive precipitable water anomalies ($>0.5\sigma$) are present across the western Caribbean, mainly east of both composite CAG genesis points. By t_0, statistically significant positive precipitable water anomalies ($>1.0\sigma$) surround the nonbaroclinic CAG center (Fig. 4c), while positive precipitable water anomalies are confined to the east of the baroclinic CAG center (Fig. 4d). In fact, negative precipitable water anomalies are mainly observed west of the composite baroclinic CAG center point (although not statistically significant). By $t_0 + 48$ h, these precipitable water anomalies in the baroclinic CAG composite have moved northeast and southwest of the CAG center, respectively (Fig. 4f), while a large circular region of positive precipitable water anomalies surrounds the nonbaroclinic CAG composite (Fig. 4e). These structural precipitable water differences between nonbaroclinic and baroclinic CAGs may be important, because the distribution of moisture can influence the amount and intensity of deep moist convection at tropical latitudes (e.g., Grabowski and Moncrieff 2004; Derbyshire et al. 2004).

Differences in the precipitable water anomalies between nonbaroclinic and baroclinic CAG categories are

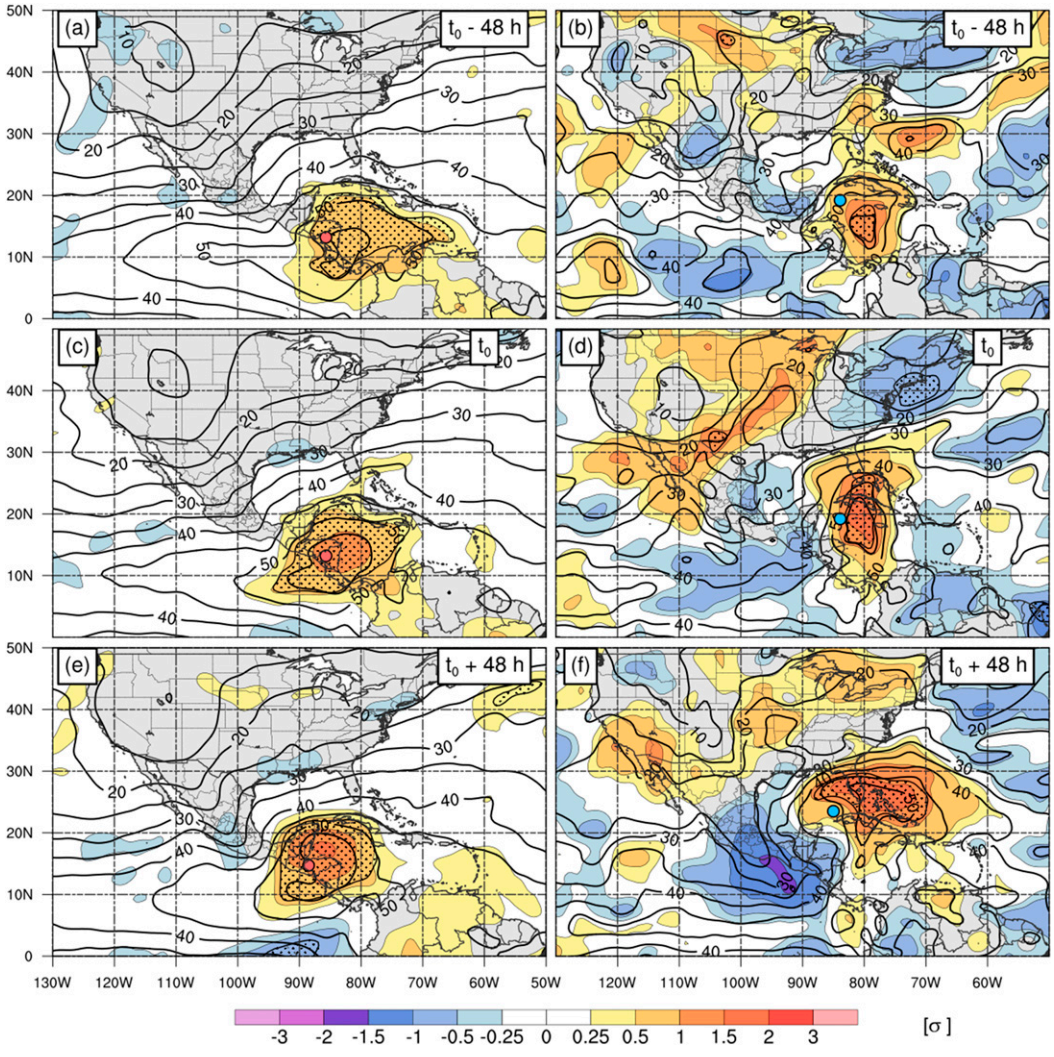

FIG. 4. As in Fig. 3, but for mean precipitable water (black contours, mm), and standardized anomalies (shaded, σ).

hypothesized to result from differences in their upper-tropospheric PV structure (Fig. 5). At t_0, nonbaroclinic CAGs have 200-hPa PV < 1 PVU within an area characterized by 500-hPa ascent ($<-1 \times 10^{-3}$ hPa s^{-1}), and anticyclonic 850–200-hPa vertical wind shear (Fig. 5a). The anticyclonic shear structure is indicative of a nonbaroclinic warm-core cyclone where the lower-tropospheric cyclone transitions into an upper-tropospheric anticyclone aloft. In contrast, baroclinic CAGs are characterized by 200-hPa PV > 2 PVU to the northwest of the CAG center, 500-hPa ascent ($<-1 \times 10^{-3}$ hPa s^{-1}) east of the CAG center, 500-hPa descent ($> 0.5 \times 10^{-3}$ hPa s^{-1}) northwest of the CAG center, and southwesterly vertical wind shear >20 m s^{-1} (Fig. 5b) over the CAG center. The strong southwesterly shear over the CAG center is associated with an upper-tropospheric PV gradient that is structurally consistent with a baroclinic cyclone. The high PV air northwest of the baroclinic CAG is associated with an upper-tropospheric trough similar to PV streamers produced via Rossby wave breaking as described in Molinari and Vollaro (2012) and Galarneau et al. (2015). This PV structure is also hypothesized to aid the ascent east of the baroclinic CAG center, because quasigeostrophic (QG) forced ascent, diagnosed via positive PV advection by the thermal wind (i.e., vertical wind shear), is present (e.g., Davis and Bosart 2003). This structure is also consistent with the heavy 24-h precipitation (>25 mm; Fig. 5f) occurring east of the AAVORT maximum. By contrast, nonbaroclinic CAGs contain a more uniform precipitation distribution in an area stretching east–west across the center (Fig. 5e). These differences in precipitation distribution may also be influenced by embedded MCSs, associated with relative vorticity maxima, which propagate around broad ML circulations (Lander 1994;

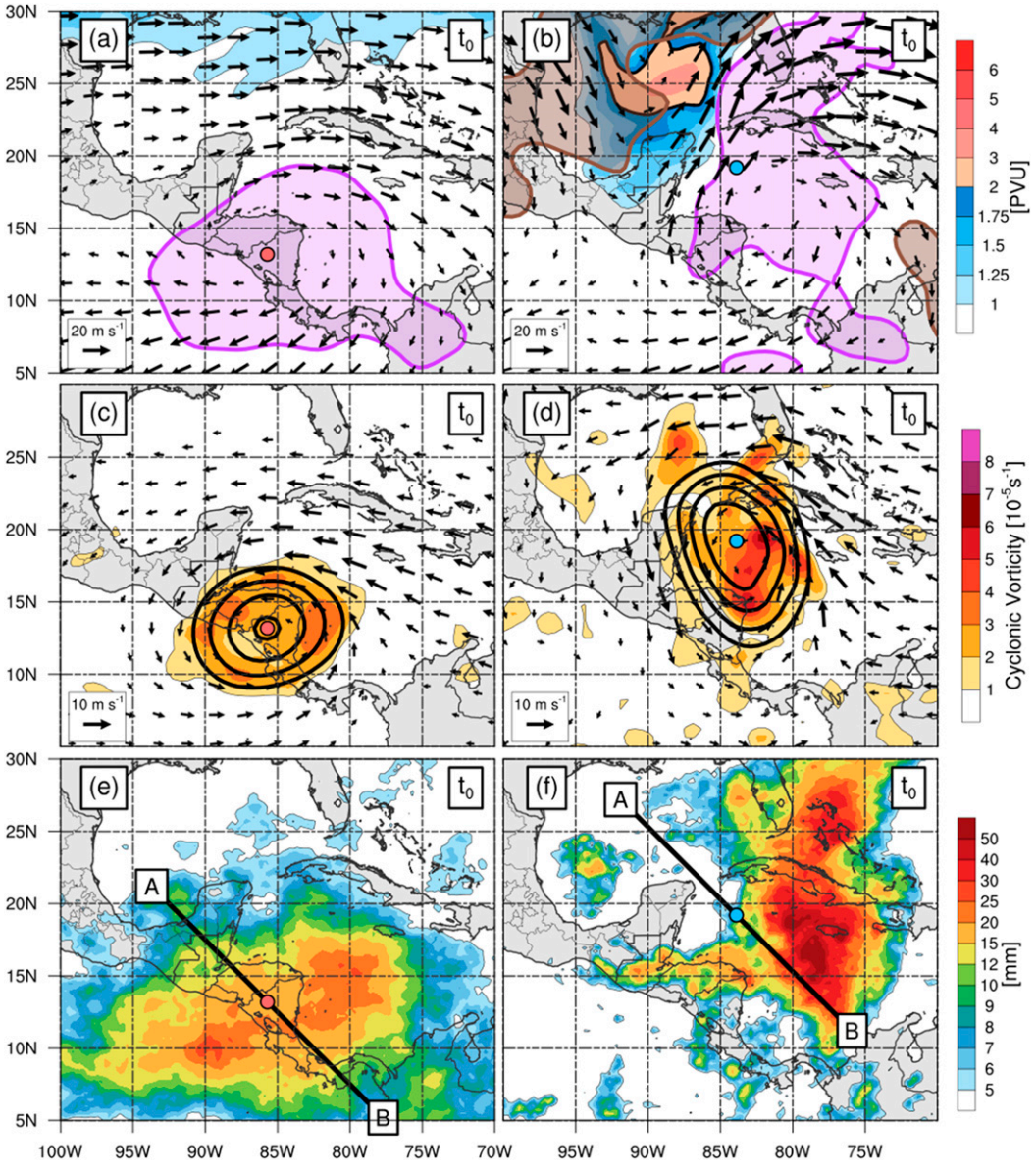

FIG. 5. (a),(b) Composite 200-hPa PV (shaded, PVU), 200–850-hPa vertical wind shear (vectors, m s^{-1}), 500-hPa ascent (purple contours with shading, $<-1 \times 10^{-3}$ hPa s^{-1}), and descent (brown contours with shading, $>0.5 \times 10^{-3}$ hPa s^{-1}) at t_0. (c),(d) Composite 850-hPa cyclonic relative vorticity (shaded, $>1 \times 10^{-5}$ hPa s^{-1}), 850-hPa AAVORT (black contours, $>1 \times 10^{-5}$ hPa s^{-1}), and 850-hPa winds (vectors, m s^{-1}) at t_0. (e),(f) Composite 24-h total precipitation (shaded, mm) t_0. (left) The nonbaroclinic CAG composite and (right) the baroclinic CAG composite. A northwest–southeast-oriented line is depicted in (e),(f) to show the location used to create cross sections in Figs. 6 and 7, respectively.

Harr et al. 1996). Nonbaroclinic CAGs maintain a uniform distribution of relative vorticity maxima around the AAVORT maximum (Fig. 5c) consistent with MCSs rotating around a MD circulation (Harr et al. 1996), while baroclinic CAGs concentrate vorticity maxima on the eastern flank of the AAVORT maximum (Fig. 5d), similar to MCSs propagating along the eastern flank of a MG circulation (Lander 1994).

Cross sections northwest–southeast through nonbaroclinic and baroclinic CAG composites also show clear vertical structural differences (Figs. 6–7). At $t_0 -$ 48 h, the composite environment of nonbaroclinic CAGs is characterized by PV < 0.25 PVU in the upper troposphere (300–200 hPa) associated with broad anticyclonic flow (Fig. 6a) and a broad positive upper-tropospheric temperature anomaly (+0.5 K), while deep tropospheric

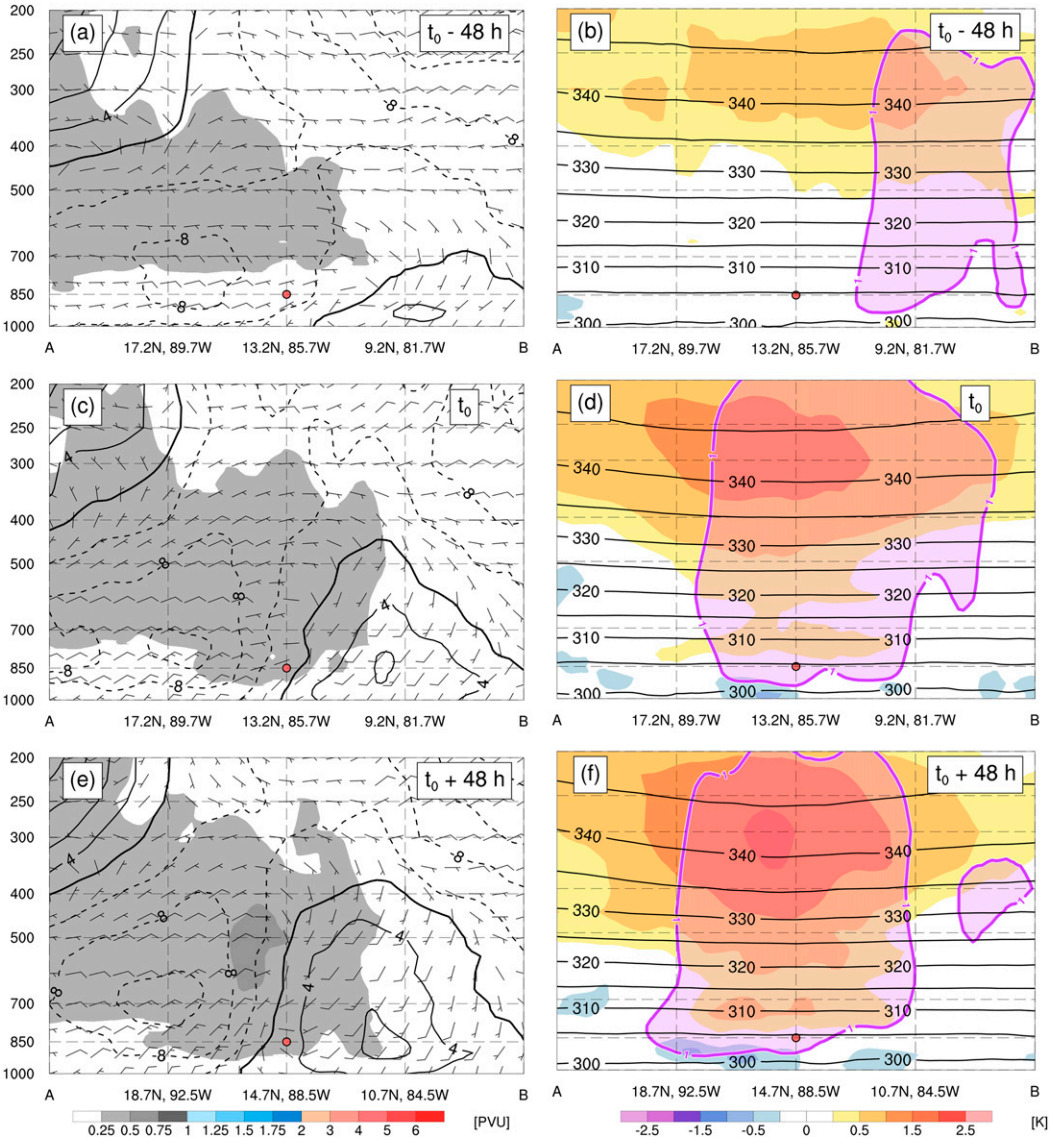

FIG. 6. Time evolution of northwest–southeast-oriented cross sections of the nonbaroclinic CAG composite at (a),(b) $t_0 - 48$ h; (c),(d) t_0; and (e),(f) $t_0 + 48$ h. (left) Potential vorticity (shaded, PVU), zonal wind [dashed (solid) black contours for easterly (westerly) winds every 4 m s^{-1}], and total wind (barbs, kt). (right) Temperature anomaly (shaded, K), potential temperature (black contours, every 5 K), and vertical ascent (purple contours with shading, $<-1 \times 10^{-3}$ hPa s^{-1}). Red circles denote the center of the nonbaroclinic CAG composite at 850 hPa. Note that cross sections shift north and west at $t_0 + 48$ h to follow the composite CAG center.

ascent occurs southeast of the CAG center (Fig. 6b). This positive temperature anomaly increases in amplitude and areal extent (maximum > 1.5 K) by t_0 (Figs. 6d,f). While not explicitly shown, this ascent is likely aiding the intensification of the upper-tropospheric warm core via condensational latent heat release. Expansion of the column by latent heat release may bow down isentropes below the level of maximum heating, stabilizing the tropospheric column below. This more stable lower- to midtropospheric column contributes to intensification of the lower- to midtropospheric PV and hence cyclonic flow (Figs. 6c,e). Above that, expansion of the column by latent heat release may bow up isentropes above the level of maximum heating, destabilizing the tropospheric column above, contributing to the destruction of the upper-tropospheric PV and enhancement of anticyclonic flow (Figs. 6c,e). The vertical composite structure of nonbaroclinic CAGs is similar to MDs (Beattie and Elsberry 2013; Boos et al. 2015; Hurley and Boos 2015), although the lower-tropospheric PV and upper-tropospheric

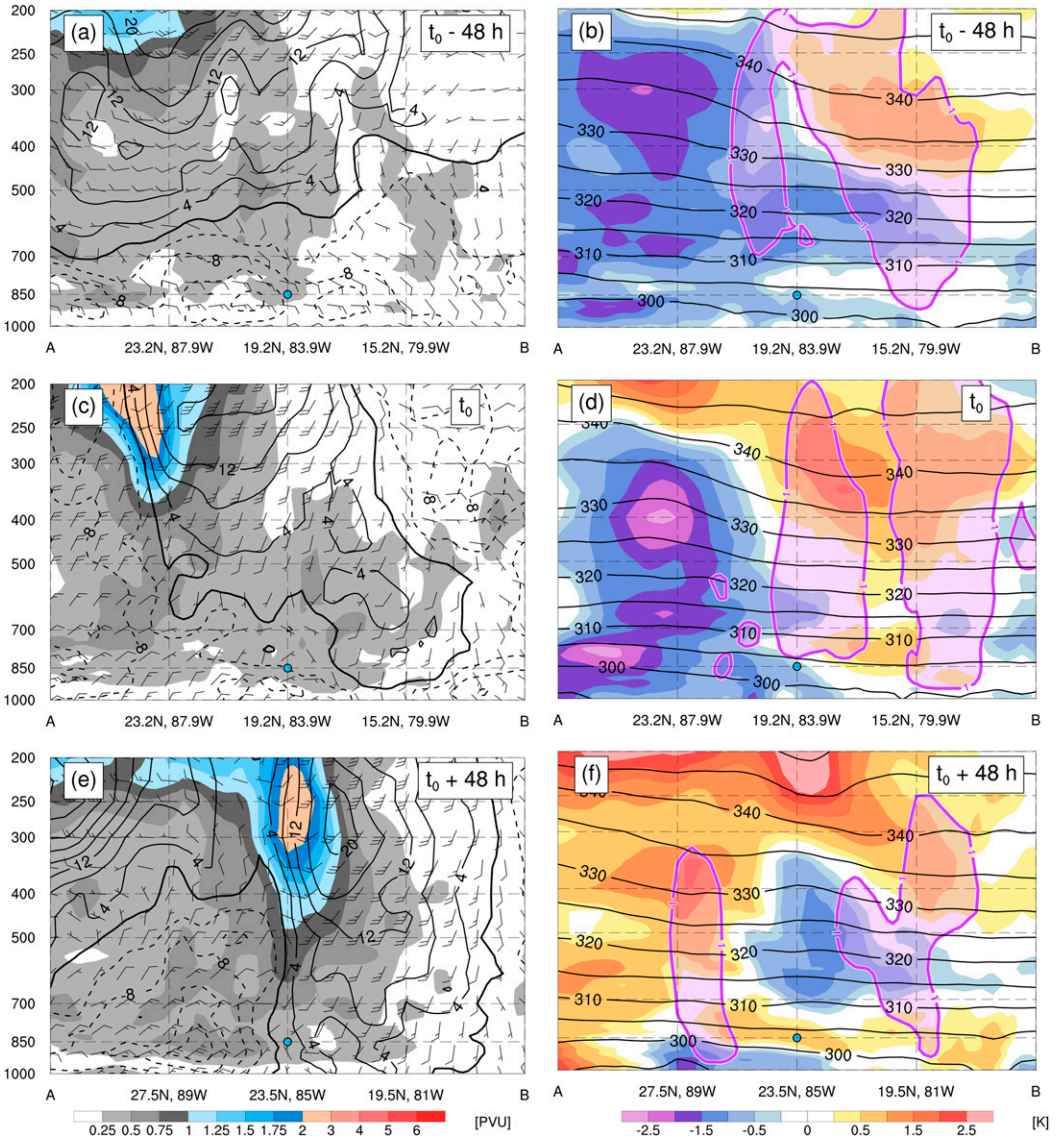

FIG. 7. As in Fig. 6, but for the baroclinic CAG composite, where blue circles denote the center of the baroclinic CAG composite at 850 hPa.

temperature anomalies are broader and not as great in magnitude as observed in eastern Pacific MDs (Hurley and Boos 2015). One possible explanation for these differences is that the Hurley and Boos (2015) composites may include TCs; in general, TCs have stronger but more confined warm cores and midtropospheric PV columns (Hawkins and Imbembo 1976).

There are notable differences in the vertical structure of baroclinic CAGs compared to nonbaroclinic CAGs (Fig. 7). At t_0 − 48 h, the composite environment of baroclinic CAGs is characterized by a northwest–southeast upper-tropospheric PV gradient (Fig. 7a), deep tropospheric ascent at and to the southeast of the CAG center (Fig. 7b), and a northwest–southeast temperature gradient (Fig. 7b). Comparing the baroclinic CAG composite to the nonbaroclinic CAG composite, the most notable difference is the broad upper-tropospheric trough northwest of the CAG center point, which is associated with a large (<-1.5 K) and expansive negative temperature anomaly. By t_0, this upper-tropospheric trough becomes more amplified and extends deeper into the troposphere (Fig. 7c). This feature is associated with the asymmetrical vertical motion and precipitation structure of the baroclinic CAG, where QG forcing (Fig. 5b) promotes ascent east of the baroclinic CAG center, and descent west of the baroclinic CAG center (Fig. 5b). These results are consistent with the structural characteristics of MG cases in Molinari and

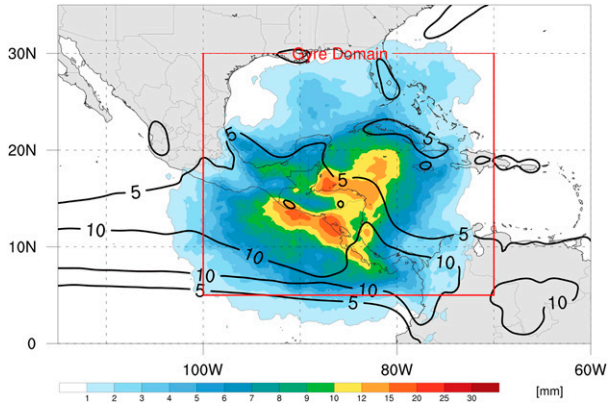

FIG. 8. Average daily rainfall rate composite for CAGs (shaded, mm day^{-1}) using rainfall observed within 10° of a CAG center compared to climatological rainfall rate during 1 May–30 Nov (black contours, every 5 mm day^{-1}).

Vollaro (2012) and Crandall et al. (2014). These MG cases are sometimes called *subtropical gyres*, because they possess a pronounced upper-tropospheric temperature gradient above their broad lower-tropospheric circulation that contributes to their cloud and moisture asymmetries. By $t_0 + 48$ h, the upper-tropospheric trough becomes superimposed on the lower-tropospheric cyclone (Fig. 7e). This vertically stacked cyclonic circulation is strongest in the upper troposphere, and that combined with negative temperature anomalies (<-0.5 K) suggest that baroclinic CAGs possess cold-core characteristics (Fig. 7f). This structure bears similarity to the MG discussed in Crandall et al. (2014, their Fig. 4), where a cutoff 200-hPa upper-tropospheric cyclone moves directly overhead of the lower-tropospheric MG circulation.

c. Rainfall

Individual CAG events are often accompanied by excessive precipitation that can result in flooding to portions of Central America and the Caribbean (Pasch and Roberts 2006; Brennan 2010; Blake 2011). Since widespread precipitation is also observed within the CAG composites (Figs. 5e–f), this section will compare composite CAG rainfall to the rainy season (May–November) climatology. In addition, CAG rainfall will be described in terms of extreme precipitation frequency and coverage.

Figure 8 compares the Earth-relative average daily rainfall of CAG events available in the PERSIANN-CDR dataset ($N = 39$) to the average daily rainfall during the rainy season. The Earth-relative framework is used here because climatological precipitation is strongly influenced by terrain over Central America; the drawback of this approach is that individual CAG rainfall areas do not always overlap, which in turn dilutes the signal. Composite daily rainfall during CAG events (>10 mm day^{-1}) exceeds the climatological rainfall rate (>5 mm day^{-1}) along the coastal regions of Central America between 95° and 80°W (Fig. 8). These results generally agree with Hurley and Boos (2015) in that ML systems are associated with enhanced rainfall. Central American coastal regions likely receive enhanced precipitation from CAGs due to their surrounding convection and upslope lower-tropospheric winds over higher topography, which often occur in large convective and stratiform precipitation events in this region (Zuluaga and Houze 2015).

CAGs are frequently associated with intense daily rainfall rates. Because of large variations in the climatological daily precipitation rate across Central America and adjacent oceans, the definition of extreme precipitation must vary in space. Here, extreme precipitation is defined as the 95th percentile of all precipitating days in the rainy season, which is a threshold that has been used in past studies (e.g., Curtis et al. 2007). Next, the number of locations within 10° of the CAG center where the daily precipitation exceeds that threshold is counted in 0.25° boxes. Not surprisingly, locations characterized by the highest CAG mean rainfall rate (Central American coastal regions along the east Pacific and Caribbean) also experience the highest number of days with extreme precipitation (Fig. 9a). Within a 10° radius of a typical CAG event, approximately 25% of grid points experience at least one day of extreme precipitation (Fig. 9b). Each CAG event observed in the PERSIANN-CDR climatology has a location (0.25° box) with at least 2 days of extreme precipitation while a large minority of CAG cases (17 out of 39, 43.6%) possess a location with at least 4 days of extreme precipitation. These statistics strongly suggest that CAG events are tied to extreme precipitation occurrence, often for multiple days in a large area, and help explain why CAG events often feature catastrophic flooding (Pasch and Roberts 2006; Brennan 2010; Blake 2011).

d. Seasonal variability

The remainder of this paper explores the bimodal seasonal peak in CAG activity and specifically the lack of CAGs during July and August (Fig. 2a). This period also coincides with a relative reduction of seasonal rainfall over Central America (i.e., *the midsummer drought*; Magaña et al. 1999). Small et al. (2007) noted that during the midsummer drought, low-level easterly wind anomalies are observed in the east Pacific equatorward of Central America, which results in moisture flux divergence near Central America. By contrast, CAGs are preceded with an extensive corridor of 850-hPa westerly wind anomalies in the same region (Fig. 3). As a consequence, one possible explanation for the lack of CAGs during July–August is that seasonal changes in the

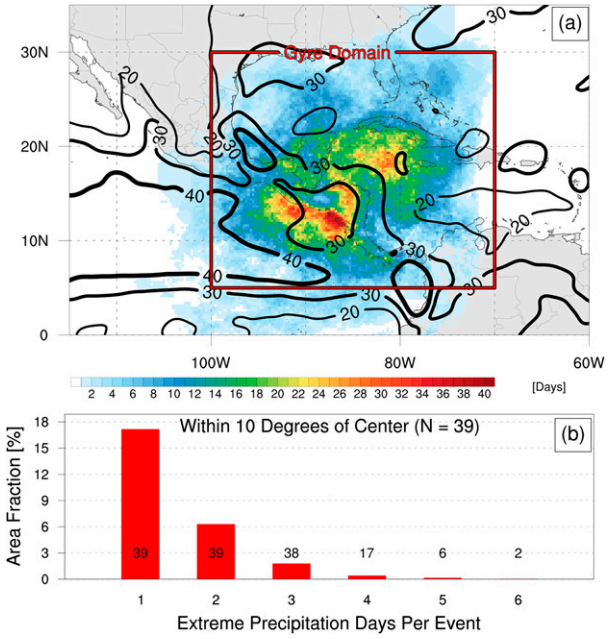

FIG. 9. (a) The number of extreme precipitation days attributed to CAG events (shaded, days) within 10° of a CAG center and the daily rainfall rate that represents the 95th percentile of all rainfall events (contours, every 10 mm day^{-1} with thickness denoting magnitude). (b) A bar graph showing the fraction of area within 10° of the CAG of extreme precipitation, where the number of extreme precipitation days is on the *x* axis and area percentage on the *y* axis. The number of CAGs that possess at least one point of extreme precipitation is labeled within.

zonal wind in the eastern Pacific adjacent to Central America are not favorable for CAG formation.

Low-level zonal winds in regions adjacent to Central America experience large changes in magnitude during the rainy season and occur in conjunction with seasonal changes in CAG occurrence. Figure 10 depicts the frequency of zonal wind during 1 May–30 November for boxes in the eastern Pacific (0°–15°N, 85°–110°W, Fig. 10a) and Caribbean Sea (10°–20°N, 60°–85°W, Fig. 10b), encompassing the statistically significant anomalies observed in Fig. 3. Not surprisingly, mean easterly zonal winds are most frequently observed in the eastern Pacific and Caribbean regions, but are weakest in May–June and September–October ($-1\,\mathrm{m\,s^{-1}}$ in the eastern Pacific and $-6\,\mathrm{m\,s^{-1}}$ in the Caribbean, respectively). Large variability about the mean exists in the eastern Pacific region, which occasionally yields westerly zonal wind with a frequency between 10% and 20% (of 48-h periods) during May–June and September–October when the mean easterly flow is weaker. These time periods coincide with all CAG events, and a majority of CAGs are preceded by westerly zonal wind in the east Pacific region (Fig. 10a). Conversely, when mean easterly zonal wind is strongest in July–August, westerly zonal winds rarely occur (frequency of $< 5\%$), which coincides with the period of no CAG events. Part of this increase in climatological easterly zonal wind in the east Pacific region is related to the extension of the Caribbean low-level jet, which peaks in magnitude in July (Shieh and Colucci 2010) and is readily seen as higher magnitude and less variable easterly zonal winds in the Caribbean region (Fig. 10b).

There are several hypotheses that may explain why westerly zonal winds in the eastern Pacific result in more favorable conditions for CAG development. One possibility is that the westerly winds provide a source of zonal kinetic energy that is converted to eddy kinetic energy via barotropic conversion (Krishnamurti et al. 1976; Aiyyer and Molinari 2008). This may manifest as the conversion of cyclonic shear vorticity into cyclonic curvature vorticity, as westerly winds equatorward of Central America (Fig. 10a) interact with easterly trade winds poleward of Central America (Fig. 10b). Another possibility is that westerly zonal winds in the eastern Pacific may trigger a series of processes that provide a source of eddy potential energy, which through diabatic processes is converted to eddy kinetic energy (Krishnamurti et al. 1976). First, the interaction of eastern Pacific westerly lower-tropospheric flow with Caribbean easterly trade winds can promote lower-tropospheric convergence over Central America. Then, if enhanced moisture preexisting near Central America (i.e., Fig. 4) overlaps with this lower-tropospheric convergence, deep moist convection can result (Fig. 5). Latent heat release associated with deep moist convection can diabatically redistribute the PV profile below, enhancing the lower-tropospheric cyclonic flow that characterizes the CAG circulation (Fig. 6). A definitive explanation for the role of the synoptic environment is beyond the scope of this study.

e. MJO

On the intraseasonal scale, an active MJO can enhance westerly zonal winds in the eastern Pacific and promote convection over Central America (Maloney and Hartmann 2000); both features that may be important to CAG development. Stratifying CAG cases by MJO RMM phase (using Wheeler and Hendon 2004) indicates a large majority of CAG cases (72.3%) occur in phases 1, 2, and 8 (Fig. 11a); which are typically associated with active convection over Central America (Wheeler and Hendon 2004). The proportion of CAG cases in these RMM phases remains consistent even when removing CAG cases associated with weak MJOs (as defined in Wheeler and Hendon 2004).

One potential reason for this MJO preference is that these MJO phases have similar planetary-scale anomalies to the CAG composites (i.e., Fig. 3). This possibility is

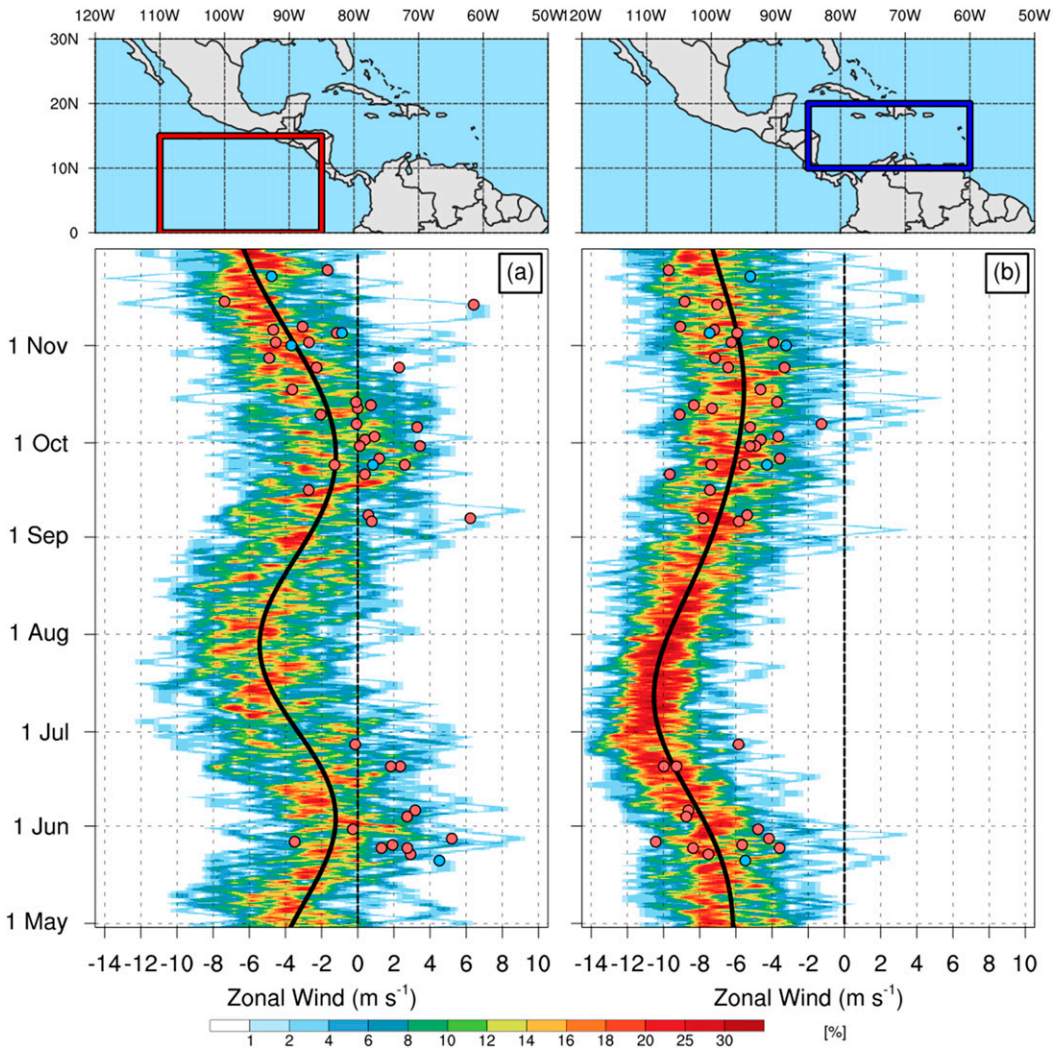

FIG. 10. The 48-h running mean 850-hPa zonal wind frequency (shaded, %) for (a) averaged over the eastern Pacific domain (0°–15°N, 110°–80°W) and (b) averaged over the Caribbean Sea domain (10°–20°N, 85°–60°W) as a function of date. The black line in (a),(b) shows the climatological zonal wind for that time period. Red and blue circles denote the zonal wind averaged 48 h before genesis of nonbaroclinic and baroclinic CAGs, respectively.

evaluated by compositing the CFSR daily 850-hPa geopotential height and wind anomalies of MJO phases associated with enhanced CAG activity during May–November (phases 1, 2, 8; $N = 3041$ days; Fig. 11b) and comparing them to the remaining MJO phases (3, 4, 5, 6; $N = 4365$ days; Fig. 11c). MJO phases 1, 2, and 8, which coincide with enhanced CAG activity, are characterized by negative height anomalies over Central America, increased height anomalies equatorward in the eastern Pacific, and westerly wind anomalies maximized in the eastern Pacific along an anomalous geopotential height gradient (Fig. 11b). By contrast, the remaining MJO phases have composite easterly wind anomalies associated with the opposite geopotential height anomaly gradient in the eastern Pacific (Fig. 11c). The low-level geopotential height and winds observed in MJO phases with enhanced CAG activity are consistent with the eastern Pacific synoptic–planetary pattern observed in Fig. 3. The MJO composite structure is also consistent with Aiyyer and Molinari (2008), where an active MJO period was associated with lower-tropospheric westerly winds in the eastern Pacific. These westerly winds aid in convergence and cyclonic relative vorticity along Central America, and are favorable factors for the development of CAGs.

4. Conclusions

The purpose of this study was to document the climatological characteristics of CAGs, which are broad lower-tropospheric cyclonic circulations that feature

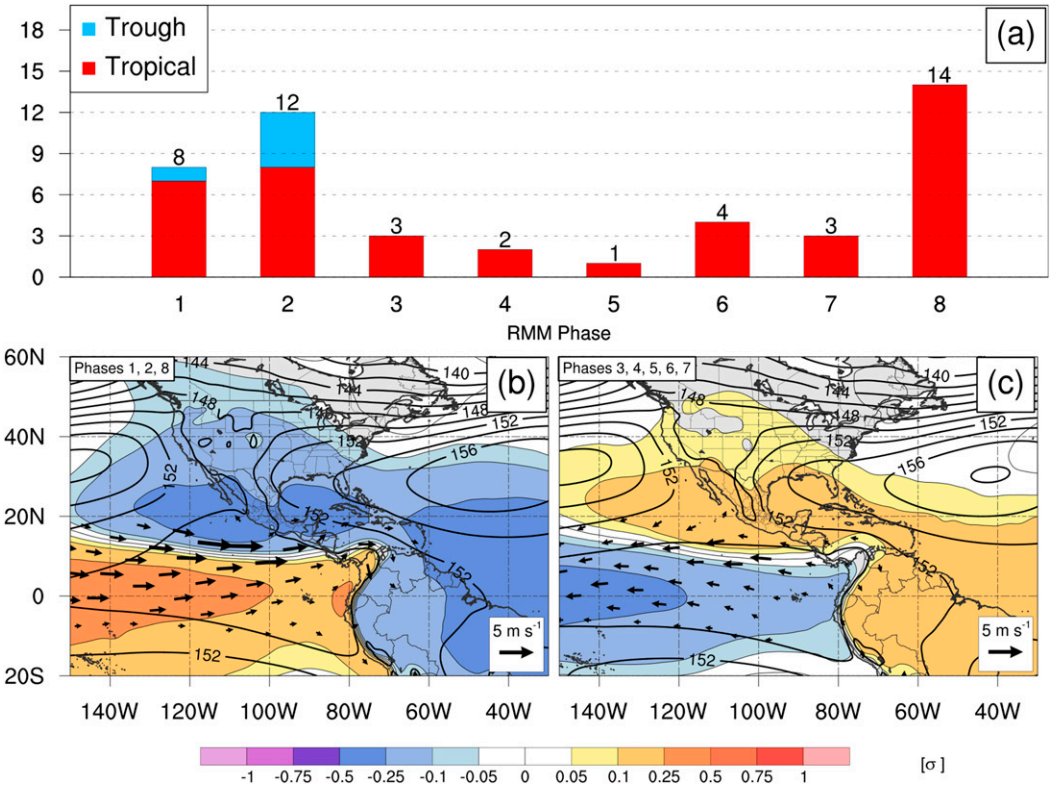

FIG. 11. (a) Bar graph of the number of CAG events in each RMM phase, where nonbaroclinic and baroclinic CAGs denoted by red and blue, respectively. (b),(c) Composite 850-hPa geopotential height (black contours, dam), standardized geopotential height anomaly (shaded, σ), and anomalous winds (vectors, m s^{-1}) for (b) MJO RMM phases 8, 1, and 2 (N = 3041 days) and (c) MJO RMM phases 3–7 (N = 4365 days) occurring during 1 May–30 Nov.

light wind cores, closed Earth-relative circulations, and widespread heavy precipitation. These systems were identified via an algorithm that evaluated area-average relatively vorticity maxima with large RMWs and closed Earth-relative circulations, which distinguish these features from TCs and open troughs. The resulting CAG cases were further stratified by the nearby upper-tropospheric (350 K) PV structure to distinguish between different types of CAG.

CAGs were identified during the rainy season in May–June and September–November with an annual frequency of 1.5 cases per year (Fig. 2a). These peaks and annual frequency of CAG activity in the present study are similar to *temporals* previously discussed in Hastenrath (1985). By contrast, Hurley and Boos (2015) identified a larger number of MDs in the same domain, with a peak in August. These differences are likely due to algorithm differences in Hurley and Boos (2015), which is more prone to identifying TCs and nonclosed vorticity features in the eastern Pacific ITCZ/MT.

Separating CAGs into nonbaroclinic and baroclinic types yields dynamically distinct structures analogous to MDs and MGs. The composite evolution of nonbaroclinic CAGs shows the development of a broad lower-tropospheric circulation and upper-tropospheric warm core, as anomalous 850-hPa westerly flow from the east Pacific (Fig. 3) converges over enhanced precipitable water near Central America (Fig. 4), promoting deep tropospheric ascent and precipitation surrounding the circulation (Fig. 5). Implied convective activity from the vertical ascent is associated with warming the upper troposphere, enhancing lower-tropospheric PV and cyclonic winds below the level of maximum heating (Fig. 6). In contrast, baroclinic CAGs have a highly asymmetrical distribution of moisture and precipitation, where enhanced precipitable water and precipitation occur to the east of an amplifying upper-tropospheric trough (Figs. 4 and 5). Ultimately, the upper-tropospheric trough becomes superimposed onto the lower-tropospheric circulation, and resembles a tropospheric cold core system (Fig. 7). Both types of CAG feature extreme precipitation over large areas for several days (Fig. 9), which can result in flooding.

The bimodal seasonal frequency of CAGs is linked to changes in the seasonal zonal winds in the eastern Pacific and the Caribbean (Fig. 10). CAGs occur most frequently in May–June and September–November, when zonal

850-hPa westerly winds in the eastern Pacific are more common (Fig. 10a). Periods of westerly zonal winds in the eastern Pacific may result in lower-tropospheric cyclonic shear vorticity, which can then be converted to cyclonic curvature vorticity over Central America. The anomalous westerly zonal wind pattern observed with CAGs is consistent with phases 1, 2, and 8 of the MJO, which coincide with a majority of CAGs (Fig. 11).

There are a number of aspects of CAGs that were not addressed here, which merit further work. It is likely that the higher topography of Central America plays a critical role in the generation and organization of convection and precipitation associated with CAG events. Moreover, gaps within the elevated terrain of Central America (Chivela Pass, Gulf of Papagayo, and Gulf of Panama) are known to generate low-level vorticity (Holbach and Bourassa 2014), which may also influence CAG organization. The CAG climatology and algorithm presented here can be applied to any region of the tropics, and may yield a different climatology relative to Hurley and Boos (2015). Future work may also investigate CAG predictability in numerical weather prediction, especially whether nonbaroclinic or baroclinic CAG events have different predictability given their tropical (MJO) or extratropical (Rossby wave breaking) influences. Finally, ML studies in the west Pacific basin have documented their influence on the motion of nearby TCs (Lander 1994; Carr and Elsberry 1995; Crandall et al. 2014). Similar interactions have been noted between CAGs and TCs (Pasch and Roberts 2006; Montgomery et al. 2012), and documenting the nature by which CAGs influence TC motion could improve TC track forecasts near CAGs.

Acknowledgments. The authors wish to thank Ms. Alicia Bentley (University at Albany), Dr. Alan Brammer (University at Albany), Mr. Brian Crandall (Atmospheric Research Science Center), Dr. Kyle Griffin (Riskpulse), Dr. Matthew Janiga (Naval Postgraduate School), Dr. John Molinari (University at Albany), and Ms. Ajda Savarin (University of Miami) for helpful discussions and research assistance. This research was funded by NSF Grant ATM-0849491 and NOAA Grant NA14OAR4830172.

REFERENCES

Aiyyer, A., and J. Molinari, 2008: MJO and tropical cyclogenesis in the Gulf of Mexico and eastern Pacific: Case study and idealized numerical modeling. *J. Atmos. Sci.*, **65**, 2691–2704, doi:10.1175/2007JAS2348.1.

Aldinger, W. T., and W. Stapler, 1998: 1998 annual tropical cyclone report. Tech. Rep. ADA381675, JTWC, U.S. Naval Pacific Meteorology and Oceanography Center, B, 224 pp.

American Meteorological Society, 2016a: Monsoon depression. Glossary of Meteorology. [Available online at http://glossary.ametsoc.org/wiki/Monsoon_depression.]

——, 2016b: Monsoon gyre. Glossary of Meteorology. [Available online at http://glossary.ametsoc.org/wiki/Monsoon_gyre.]

Ashouri, H., K. L. Hsu, S. Sorooshian, D. K. Braithwaite, K. R. Knapp, L. D. Cecil, B. R. Nelson, and O. P. Prat, 2015: PERSIANN-CDR: Daily precipitation climate data record from multisatellite observations for hydrological and climate studies. *Bull. Amer. Meteor. Soc.*, **96**, 69–83, doi:10.1175/BAMS-D-13-00068.1.

Baray, J.-L., G. Clain, M. Plu, E. Feld, and P. Caroff, 2010: Occurrence of monsoon depressions in the Southwest Indian Ocean: Synoptic descriptions and stratosphere to troposphere exchange investigations. *J. Geophys. Res.*, **115**, D17108, doi:10.1029/2009JD013390.

Beattie, J. C., and R. L. Elsberry, 2013: Horizontal structure of monsoon depressions in the western North Pacific at formation time. *Geophys. Res. Lett.*, **40**, 983–987, doi:10.1002/grl.50198.

Blake, E. S., 2011: Tropical Cyclone Report: Tropical Storm Nicole (28–29 September 2010). Tech. Rep. AL162010, National Hurricane Center, 15 pp. [Available online at http://www.nhc.noaa.gov/data/tcr/AL162010_Nicole.pdf.]

Boos, W. R., J. V. Hurley, and V. S. Murthy, 2015: Adiabatic westward drift of Indian monsoon depressions. *Quart. J. Roy. Meteor. Soc.*, **141**, 1035–1048, doi:10.1002/qj.2454.

Brennan, M. J., 2010: Tropical Cyclone Report: Tropical Storm Matthew (23–26 September 2010). Tech. Rep. AL152010, National Hurricane Center, 15 pp. [Available online at http://www.nhc.noaa.gov/data/tcr/AL152010_Matthew.pdf.]

Carr, L. E., and R. L. Elsberry, 1995: Monsoonal interactions leading to sudden tropical cyclone track changes. *Mon. Wea. Rev.*, **123**, 265–290, doi:10.1175/1520-0493(1995)123<0265:MILTST>2.0.CO;2.

Chen, T.-C., and S.-P. Weng, 1999: Interannual and intraseasonal variations in monsoon depressions and their westward-propagating predecessors. *Mon. Wea. Rev.*, **127**, 1005–1020, doi:10.1175/1520-0493(1999)127<1005:IAIVIM>2.0.CO;2.

——, S.-Y. Wang, M.-C. Yen, and W. A. Gallus, 2004: Role of the monsoon gyre in the interannual variation of tropical cyclone formation over the western North Pacific. *Wea. Forecasting*, **19**, 776–785, doi:10.1175/1520-0434(2004)019<0776:ROTMGI>2.0.CO;2.

Crandall, B., 2012: An analysis of the formation and evolution of the 1989 western North Pacific subtropical gyre. M.S. thesis, Dept. of Atmospheric and Environmental Sciences, University at Albany, State University of New York, 91 pp.

——, J. Molinari, and D. Vollaro, 2014: Forecasting challenges associated with tropical cyclones within subtropical gyres. *Wea. Forecasting*, **29**, 99–114, doi:10.1175/WAF-D-13-00053.1.

Curtis, S., A. Salahuddin, R. F. Adler, G. J. Huffman, G. Gu, and Y. Hong, 2007: Precipitation extremes estimated by GPCP and TRMM: ENSO relationships. *J. Hydrometeor.*, **8**, 678–689, doi:10.1175/JHM601.1.

Davidson, N. E., and G. J. Holland, 1987: A diagnostic analysis of two intense monsoon depressions over Australia. *Mon. Wea. Rev.*, **115**, 380–392, doi:10.1175/1520-0493(1987)115<0380:ADAOTI>2.0.CO;2.

Davis, C. A., and L. F. Bosart, 2003: Baroclinically induced tropical cyclogenesis. *Mon. Wea. Rev.*, **131**, 2730–2747, doi:10.1175/1520-0493(2003)131<2730:BITC>2.0.CO;2.

Dee, D. P., and Coauthors, 2011: The ERA-Interim reanalysis: Configuration and performance of the data assimilation system. *Quart. J. Roy. Meteor. Soc.*, **137**, 553–597, doi:10.1002/qj.828.

Derbyshire, S. H., I. Beau, P. Bechtold, J. Grandpeix, J. Piriou, J. Redelsperger, and P. M. M. Soares, 2004: Sensitivity of moist convection to environmental humidity. *Quart. J. Roy. Meteor. Soc.*, **130**, 3055–3079, doi:10.1256/qj.03.130.

Douglas, M. W., 1992: Structure and dynamics of two monsoon depressions. Part I: Observed structure. *Mon. Wea. Rev.*,

120, 1524–1547, doi:10.1175/1520-0493(1992)120<1524:SADOTM>2.0.CO;2.

Eliot, J., 1900: *Hand Book of Cyclonic Storms in the Bay of Bengal for the Use of Sailors.* 2nd ed. Meteorological Department of the Government of India, Calcutta, India, 316 pp.

Fernandez, W., and J. A. Barrantes, 1996: The Central American temporal: A long-lived tropical rain-producing system. *Top. Meteor. Oceanogr.*, **3** (2), 73–88.

Galarneau, T. J., R. McTaggart-Cowan, L. F. Bosart, and C. A. Davis, 2015: Development of North Atlantic tropical disturbances near upper-level potential vorticity streamers. *J. Atmos. Sci.*, **72**, 572–597, doi:10.1175/JAS-D-14-0106.1.

Godbole, R. V., 1977: The composite structure of the monsoon depression. *Tellus*, **29A**, 25–40, doi:10.3402/tellusa.v29i1.11327.

Grabowski, W. W., and M. W. Moncrieff, 2004: Moisture–convection feedback in the tropics. *Quart. J. Roy. Meteor. Soc.*, **130**, 3081–3104, doi:10.1256/qj.03.135.

Harr, P. A., R. L. Elsberry, and J. C. L. Chan, 1996: Transformation of a large monsoon depression to a tropical storm during TCM-93. *Mon. Wea. Rev.*, **124**, 2625–2643, doi:10.1175/1520-0493(1996)124<2625:TOALMD>2.0.CO;2.

Hastenrath, S., 1985: *Climate and Circulation of the Tropics.* 1st ed. D. Reidel Publishing Company, 455 pp.

Hawkins, H. F., and S. M. Imbembo, 1976: The structure of a small, intense hurricane—Inez 1966. *Mon. Wea. Rev.*, **104**, 418–442, doi:10.1175/1520-0493(1976)104<0418:TSOASI>2.0.CO;2.

Hodges, K. I., 1995: Feature tracking on the unit-sphere. *Mon. Wea. Rev.*, **123**, 3458–3465, doi:10.1175/1520-0493(1995)123<3458:FTOTUS>2.0.CO;2.

Holbach, H. M., and M. A. Bourassa, 2014: The effects of gap-wind-induced vorticity, the monsoon trough, and the ITCZ on east Pacific tropical cyclogenesis. *Mon. Wea. Rev.*, **142**, 1312–1325, doi:10.1175/MWR-D-13-00218.1.

Holland, G. J., 1995: Scale interaction in the western Pacific monsoon. *Meteor. Atmos. Phys.*, **56**, 57–79, doi:10.1007/BF01022521.

Holton, J. R., 2004: *An Introduction to Dynamic Meteorology.* 4th ed. Elsevier Academic Press, 535 pp.

Hurley, J. V., and W. R. Boos, 2015: A global climatology of monsoon low pressure systems. *Quart. J. Roy. Meteor. Soc.*, **141**, 1049–1064, doi:10.1002/qj.2447.

Kimball, S. K., and M. S. Mulekar, 2004: A 15-year climatology of North Atlantic tropical cyclones. Part I: Size parameters. *J. Climate*, **17**, 3555–3575, doi:10.1175/1520-0442(2004)017<3555:AYCONA>2.0.CO;2.

Knapp, K. R., and Coauthors, 2011: Globally gridded satellite observations for climate studies. *Bull. Amer. Meteor. Soc.*, **92**, 893–907, doi:10.1175/2011BAMS3039.1.

Krishnamurti, T. N., M. Kanamitsu, R. Godbole, C.-B. Chang, F. Carr, and J. H. Chow, 1975: Study of a Monsoon Depression (I) Synoptic Structure. *J. Meteor. Soc. Japan*, **53**, 227–240.

——, ——, ——, ——, ——, and ——, 1976: Study of a Monsoon Depression (II) Dynamical Structure. *J. Meteor. Soc. Japan*, **54** (4), 208–225.

Lander, M. A., 1994: Description of a monsoon gyre and its effects on the tropical cyclones in the western North Pacific during August 1991. *Wea. Forecasting*, **9**, 640–654, doi:10.1175/1520-0434(1994)009<0640:DOAMGA>2.0.CO;2.

Lawrence, M. B., 1998: Tropical Cyclone Report: Tropical Storm Frances. Tech. Rep. AL061998, National Hurricane Center, 8 pp. [Available online at http://www.nhc.noaa.gov/data/tcr/AL061998_Frances.pdf.]

Madden, R. A., and P. R. Julian, 1971: Detection of a 40–50-day oscillation in the zonal wind in the tropical Pacific. *J. Atmos. Sci.*, **28**, 702–708, doi:10.1175/1520-0469(1971)028<0702:DOADOI>2.0.CO;2.

Magaña, V., J. A. Amador, and S. Medina, 1999: The mid-summer drought over Mexico and Central America. *J. Climate*, **12**, 1577–1588, doi:10.1175/1520-0442(1999)012<1577:TMDOMA>2.0.CO;2.

Maloney, E. D., and D. L. Hartmann, 2000: Modulation of hurricane activity in the Gulf of Mexico by the Madden-Julian Oscillation. *Science*, **287**, 2002–2004, doi:10.1126/science.287.5460.2002.

Molinari, J., and D. Vollaro, 2012: A subtropical cyclonic gyre associated with interactions of the MJO and the midlatitude jet. *Mon. Wea. Rev.*, **140**, 343–357, doi:10.1175/MWR-D-11-00049.1.

Montgomery, M. T., and Coauthors, 2012: The Pre-Depression Investigation of Cloud-Systems in the Tropics (PREDICT) Experiment: Scientific basis, new analysis tools, and some first results. *Bull. Amer. Meteor. Soc.*, **93**, 153–172, doi:10.1175/BAMS-D-11-00046.1.

Mooley, D., and J. Shukla, 1987: Characteristics of the westward moving summer monsoon low pressure systems over the Indian region and their relationship with the monsoon rainfall. Tech. Rep., Center for Ocean–Land–Atmosphere Interactions, University of Maryland, College Park, MD, 218 pp. [Available online at http://cola.gmu.edu/people/Shukla's%20Articles/1988/Characteristics.pdf.]

Pasch, R. J., and D. P. Roberts, 2006: Tropical Cyclone Report: Hurricane Stan 1–5 October 2005. Tech. Rep. AL202005, National Hurricane Center, 12 pp. [Available online at http://www.nhc.noaa.gov/data/tcr/AL202005_Stan.pdf.]

——, L. A. Avila, and J. L. Guiney, 2001: Atlantic hurricane season of 1998. *Mon. Wea. Rev.*, **129**, 3085–3123, doi:10.1175/1520-0493(2001)129<3085:AHSO>2.0.CO;2.

Piddington, H., 1876: *Sailor's Horn-Book for the Law of Storms.* 6th ed. Williams & Norgate, London, England, 452 pp.

Saha, S., and Coauthors, 2010: The NCEP Climate Forecast System Reanalysis. *Bull. Amer. Meteor. Soc.*, **91**, 1015–1057, doi:10.1175/2010BAMS3001.1.

Sanders, F., 1984: Quasi-geostrophic diagnosis of the monsoon depression of 5–8 July 1979. *J. Atmos. Sci.*, **41**, 538–552, doi:10.1175/1520-0469(1984)041<0538:QGDOTM>2.0.CO;2.

Schenkel, B. A., and R. E. Hart, 2012: An examination of tropical cyclone position, intensity, and intensity life cycle within atmospheric reanalysis datasets. *J. Climate*, **25**, 3453–3475, doi:10.1175/2011JCLI4208.1.

Shieh, O. H., and S. J. Colucci, 2010: Local minimum of tropical cyclogenesis in the eastern Caribbean. *Bull. Amer. Meteor. Soc.*, **91**, 185–196, doi:10.1175/2009BAMS2822.1.

Small, R. J. O., S. P. De Szoeke, and S.-P. Xie, 2007: The Central American midsummer drought: Regional aspects and large-scale forcing. *J. Climate*, **20**, 4853–4873, doi:10.1175/JCLI4261.1.

Wheeler, M. C., and H. H. Hendon, 2004: An all-season real-time multivariate MJO index: Development of an index for monitoring and prediction. *Mon. Wea. Rev.*, **132**, 1917–1932, doi:10.1175/1520-0493(2004)132<1917:AARMMI>2.0.CO;2.

Wu, L., H. Zong, and J. Liang, 2013: Observational analysis of tropical cyclone formation associated with monsoon gyres. *J. Atmos. Sci.*, **70**, 1023–1034, doi:10.1175/JAS-D-12-0117.1.

Yoon, J.-H., and T.-C. Chen, 2005: Water vapor budget of the Indian monsoon depression. *Tellus*, **57A**, 770–782, doi:10.1111/j.1600-0870.2005.00145.x.

Zuluaga, M. D., and R. A. Houze Jr., 2015: Extreme convection of the near-equatorial Americas, Africa, and adjoining oceans as seen by TRMM. *Mon. Wea. Rev.*, **143**, 298–316, doi:10.1175/MWR-D-14-00109.1.